# PROCEEDINGS OF SPIE

# Shack-Hartmann wavefront sensor precision and accuracy

Daniel R. Neal, James  Copland, David A. Neal

**SPIE.**

# Shack-Hartmann wavefront sensor precision and accuracy

Daniel R. Neal, James Copland, David Neal

WaveFront Sciences, Inc., 14810 Central S.E., Albuquerque, NM 87123

## ABSTRACT

The design of a wavefront sensor may be determined by the lenslet array and camera selection. There are numerous different applications for these sensors, requiring widely differing dynamic range and accuracy. Performance metrics are needed to evaluate candidate designs and to compare results. We have developed a standard methodology for measuring the repeatability, accuracy and dynamic range of different wavefront sensor designs, and have experimentally applied these metrics to a number of different sensors.

Keywords: Shack-Hartmann, Hartmann-Shack, wavefront sensor, Hartmann sensor, adaptive optics, aberrometer, interferometer, wavefront sensing, error analysis

## 1. INTRODUCTION

As an alternative to interferometry, the Shack-Hartmann wavefront sensor is simple, compact, robust, and relatively vibration insensitive. It makes passive measurements of the incident light, can be arranged to and is wavelength-independent. These advantages have led to a large number of new applications that were previously much more expensive or difficult.

The Shack-Hartmann wavefront sensor has been applied to adaptive optics for high-energy lasers and astronomy for many years.[1] However, as the technology has matured, its techniques have been adapted to many other fields. Early sensors based on crude lenslet arrays were found to be surprisingly accurate. This quickly led to the development of more sophisticated sensors focused around modern computers, CCD cameras, and micro-optics. One of the earliest applications was the measurement of high-speed dynamic phenomena such as turbulence or fluid motion. But over time, applications in ophthalmology, quality laser beam measurement, optics testing, and optical system alignment have been introduced.

The quality of the laser beam has been an important factor for many years. The Shack-Hartmann wavefront sensor has been applied to this problem because it provides a simultaneous phase and irradiance distribution measurement that does not rely on an external reference. Using this technique, the RMS wavefront error, beam Strehl ratio, and near and far-field propagation can be routinely measured. Even $M^2$, along with other beam parameters, can be determined in a single measurement.[2,3]

With the simple expedient of bouncing a light source from a surface, the metrology of the surface can be measured with the Shack-Hartmann wavefront sensor. This has facilitated a number of other applications.[4] Geometry similar to that of an interferometer can readily be constructed to test flats, powered optics, and other elements. The Shack-Hartmann wavefront sensor can be built with a dynamic range hundreds or thousands of times larger than a conventional interferometer. Because the sensor measures the incident light, transmissive elements can be measured directly, rather than indirectly. In some cases, this simplifies the measurement arrangement.[5]

One key example of these applications is the measurement of the aberrations of the eye. This field has been revolutionized in the last few years by the introduction of the Shack-Hartmann wavefront aberrometer. While these systems were initially very similar to those used for astronomical adaptive optics, they have become increasingly sophisticated.[6,7] There are now various commercial instruments that are used to measure the eye and even provide information that is used for custom Lasik or PRK.[8] The new information about the higher order aberrations of the eye has significantly improved the results that are now routinely achieved by the Lasik and PRK procedures.

One feature that makes the Shack-Hartmann wavefront sensor so useful is that the precision and accuracy can be scaled over a huge range through the choice of lenslet array and detector. For the ophthalmic applications, the accuracy does not typically need to be better than $\lambda/10$. However, the aberrations can easily be hundreds of waves. These sensors have been designed to handle measurements containing extremely large wavefront errors. On the other hand, there are applications that require extremely high accuracy yet do not have a requirement for large

dynamic range. An example of this is measurement of the nanotopography of silicon wafers used in the semiconductor industry. In this case, extremely small variations in the surface structure (with depths on the order of 5–10 nm) can lead to a failure of the patterned device late in the manufacturing process. Thus it is important to detect these in the silicon wafer substrate prior to fabrication. This requires extreme accuracy and large dynamic range due to the natural bow and warp of these very thin but large-diameter substrates. A new Shack-Hartmann based nanotopography system has recently proven to be very effective at this type of measurement. [9]

For all of these instruments and applications, it is important to establish the precision, accuracy, and dynamic range of the different sensors. If a key advantage of this type of sensor is the scalability to different precision and accuracy, then we need methods for designing the sensor and for measuring the resulting performance. In this paper, we will introduce a basic design methodology, define the various terms, and show example methods for measuring the performance of Shack-Hartmann wavefront sensor systems.

## 2. MEASUREMENT PRINCIPLES

The basic geometry of a Shack-Hartmann[*] based sensor is described in Figure 1. The sensor consists of two basic parts: a lenslet array and a position-sensing detector. The Hartmann geometry is very similar to this except that a grid of holes replaces the lenslet array. The incoming light is dissected into a number of small samples by the lenslet array, which then focuses the light onto the detector array. A wide variety of methods for fabricating lenslet arrays have been used. Early examples were built through the juxtaposition of a number of small lenslets glued or fixed in an assembly. The use of binary optics and other micro-optics technology has greatly improved the accuracy, resolution, and fill factor of the lenslet array. There is a whole art devoted to the design, fabrication, and characterization of such elements[10] that is beyond the scope of this



**Figure 1 – Basic layout of Shack-Hartmann wavefront sensor.**

paper. The lenslet array thus creates a number of separated focal spots of light on the detector. The key principle is that the position of these focal spots is directly related to the average wavefront slope across the lenslet. Thus a measurement of the focal spot position uniquely determines the wavefront slope for that sample if the other system parameters are known.
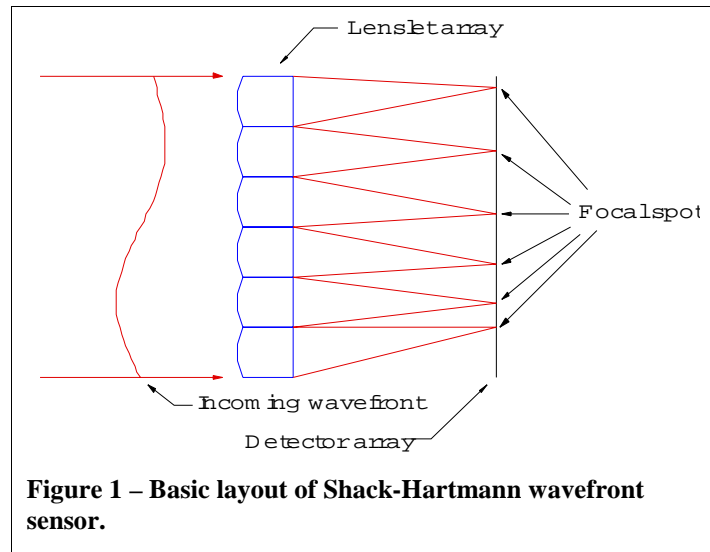
A position-sensing detector determines the focal spot position. Commonly, a CCD detector is used for this purpose. This allows a flexible measurement since it allows even dynamic allocation of detector pixels to the focal spots. An algorithm that processes the detected image and locates the focal spots determines the focal spot position. The wavefront slopes are computed by comparison to a reference and the wavefront through reconstruction from the array of wavefront slopes.

There are three basic steps to the analysis process: determination of the spot positions, conversion to wavefront slopes, and wavefront reconstruction.

### 2.1. Spot position

For a pixilated sensor, the location of the focal spots is determined from the light distribution on the detector array. For a sampled irradiance distribution with measured pixel intensities $E_{ij}$, the spot positions $x_{c,k}$ and $y_{c,k}$ are commonly determined by the first moments:

---

[*] While we use the term Shack-Hartmann sensor, many other authors prefer to use the term Hartmann-Shack. This is strictly a choice of terminology. The authors think of this as the Shack modified Hartmann sensor, hence the Shack-Hartmann sensor. However, the chronological order would support Hartmann-Shack as the preferred term. While Hartmann dates from about 1900, the modern incarnation of this sensor, using a position sensitive detector and a lenslet array was introduced by Roland Shack and Ben Platt in 1971[1].

$$x_{c,k} = \frac{\sum\limits_{i,j \in AOI_k} x_{i,j} I_{i,j}}{\sum\limits_{i,j \in AOI_k} I_{i,j}} \quad \text{and} \quad y_{c,k} = \frac{\sum\limits_{i,j \in AOI_k} y_{i,j} I_{i,j}}{\sum\limits_{i,j \in AOI_k} I_{i,j}} \tag{1}$$

where the index $k$ is over the lenslet number with center position $(x_l, y_l)_k$ and the summation is taken over the pixels assigned to the lenslet $k$, in Area-of-Interest $AOI_k$.[11] There are a number of variations to this, including thresholding or image deconvolution, that affect the accuracy of this determination. All of these methods result in the estimation of the position of the focal spots across the array. Quite often these techniques are called centroiding, with the focal-spot positions called the "centroids."[†] One key objective of this paper is to detail methods that can be used to describe the precision and accuracy of these various centroiding methods.

## 2.2.  Wavefront slope

The wavefront slope distribution is determined by comparison of the measured centroids to a reference wavefront. The reference can be determined only from the positions of the lenslet centers, but more commonly it is recorded using a reference wavefront measured with the wavefront sensor system. For a set of measured centroids $(x_c, y_c)_k$ and reference centroids $(x_r, y_r)_k$, the wavefront slope distribution is:

$$\begin{pmatrix} \langle \partial w/\partial x \rangle \\ \langle \partial w/\partial y \rangle \end{pmatrix}_k = \begin{pmatrix} \beta_x \\ \beta_y \end{pmatrix}_k \approx \frac{1}{L_H} \begin{pmatrix} x_c - x_r \\ y_c - y_r \end{pmatrix}_k . \tag{2}$$

where $L_H$, the distance between the lenslet array and detector, is normally set to the lenslet focal length, $f$.

## 2.3.  Wavefront reconstruction

The wavefront is related to the slope through the definition of the gradient:

$$\nabla w = \frac{\partial w}{\partial x} \hat{i} + \frac{\partial w}{\partial y} \hat{j} \tag{3}$$

Note that this equation describes the gradient of the wavefront in terms of the local derivatives. In a practical SHWFS, the local derivatives are approximated by the average over the lenslet area. For a large diameter lenslet this may be an additional source of error, which, in some situations, can be significant.[12] See section 3.2.3 for more details.

There are a number of different methods for reconstructing the wavefront from the slope measurements. Two basic types of methods are commonly used: zonal (direct numerical integration) and modal (polynomial fitting).[13] There are many different implementations of these integration methods described in the literature; two representative examples are given below.

### 2.3.1.  Zonal

One method for reconstructing the wavefront is to write the wavefront gradients in terms of finite-differences and to numerically integrate the data. Since the integration is performed zone by zone (lenslet by lenslet), this is called the zonal method. The measured wavefront slopes can be approximated by the finite difference:

$$\beta_0^x = \frac{1}{2d_x} \left[ w(x_0 + d_x) - w(x_0 - d_x) \right] \equiv \frac{1}{2d_x} \left( w_1 - w_{-1} \right) \tag{4}$$

where 0, +1 and −1 subscripts describe the wavefront at the adjoining lenslet locations. The wavefront can be written:

---

[†] The mathematical definition of the centroid refers to the center of the distribution of the given shape with no variation in the weighting. Since the pixelized intensity is most often used as the weighting function, this is technically not quite the right term. However, the other common term, "center-of-mass" seems inappropriate as well given that there is no mass involved in any of the parameters. The term "centroid" in common use in the wavefront sensor literature refers to the spot positions determined through some numerical or analytic method.

$$w_{i+1,j} = w_{i-1,j} + 2d_x\beta_{i,j}^x \text{ and } w_{i,j+1} = w_{i,j-1} + 2d_y\beta_{i,j}^y \tag{5}$$

This equation can be solved by marching through the data, through least-squares fitting or through iterative methods. The boundary conditions play an important part in the accurate determination of the wavefront from the slope data[13].

### 2.3.2. Modal

In the modal reconstruction method, the wavefront is described in terms of functions that have analytic derivatives. The measured slope data is then fit to the derivative of these functions, allowing a direct determination of the wavefront from the fit coefficients. That is, if the wavefront at point $(x,y)$ is written as an expansion in terms of polynomials $P_m(x,y)$:

$$w(x, y) = \sum_{m=1}^{M} C_m P_m(x, y) \tag{6}$$

then the local wavefront slopes can be written as:

$$\begin{pmatrix} \partial w/\partial x \\ \partial w/\partial y \end{pmatrix}_k = \begin{pmatrix} \sum_{m=2}^{M} C_m \dfrac{\partial P_m}{\partial x} \\ \sum_{m=2}^{M} C_m \dfrac{\partial P_m}{\partial y} \end{pmatrix} \tag{7}$$

The sum-squares is written:

$$\chi^2 = \sum_k \left( \beta_k^x - \sum_{m=2}^{M} C_m \frac{\partial P_m}{\partial x} \right)^2 + \sum_k \left( \beta_k^y - \sum_{m=2}^{M} C_m \frac{\partial P_m}{\partial y} \right)^2 \tag{8}$$

This can be minimized by setting:

$$\frac{\partial \chi^2}{\partial C_m} = 0 \tag{9}$$

and solving the resulting system of equations. In practice, the polynomials that are used are often orthogonal polynomials such as Zernike, or Tschebychev polynomials. The non-orthogonal set of Taylor polynomials is also frequently used.

## 3. SOURCES OF UNCERTAINTY

There are several different sources of uncertainty and error in the wavefront sensor process. It is important to understand these different contributors in designing a system and in interpreting the results. Several authors have described the statistical uncertainty of a Shack-Hartmann wavefront sensor in various conditions.[14,15]

### 3.1. Alignment and calibration

Pfund et al[16] have considered the various alignment and calibration effects that contribute to systematic errors of the system. The effect of lenslet rotation, tip, tilt, and other alignment effects were carefully considered. Several of these parameters were shown to have a significant effect on the accuracy of the measurements. If the reference centroids are recorded using an ideal light source, it is possible to subtract some of these effects. This results from the fact that the measurements are essentially differential, so as long as the lenslet array rotation and alignment are preserved, there is little systematic error. However, lenslet array tip and tilt could significantly affect the system accuracy, so care is required to maintain proper lenslet array alignment, at least within mechanical tolerances.

One important parameter is the distance between the lenslet array and the detector. This distance must be precisely known to avoid a calibration offset. This can be calibrated by recording a number of known wavefronts and then comparing them against the measurement made by the WFS.

## 3.2. Repeatability and accuracy of wavefront sensor numerical analysis

The precision and accuracy of the wavefront sensor measurements in general are quite different. This depends upon the particular geometry of the lenslet array and detector combination.

Precision is defined as the repeatability of the sensor. That is, given an unchanging incident wavefront, precision is the variation (usually expressed in terms of a root-mean-square value) in the resulting measurement. Finite precision comes about as a result of pixelization, detector signal to noise ratio, CCD readout noise, frame grabber line or synch jitter, and other random or time dependent effects.

Sensor accuracy is defined as the ability of the sensor to measure a given known wavefront. Finite accuracy comes about as a result of finite pixelization, cross-talk between lenslets, out-of-range conditions, background light, spot motion during the exposure time, light incident during the CCD readout (for full-frame CCDs), and several other effects.

It is quite important to distinguish between these two sources of uncertainty. For a wavefront sensor system where the focal spot covers a fairly small number of pixels, the repeatability can be quite good. For example, with a 144 μm diameter, 8mm focal length lenslet array, the focal spot covers about 6×6 pixels. Even with an 8-bit CCD, the S/N is usually greater than 100:1. Since there are 36 pixels involved in the centroid calculation, the S/N of the centroid algorithm can be nearly 600:1. This leads (for this example) to a precision of better than 0.1 μm in estimating the location of the focal spot (about 1/100th of a pixel).

However, this is only part of the story. With this same system, if the focal spot is moved systematically across the CCD, a systematic error of up to 2 μm (1/5th pixel) would be observed. This pattern is systematic for an individual focal spot, but varies randomly across the lenslet array due to a mismatch between the lenslet array spacing or alignment relative to the detector array. This limits the accuracy with which it is possible to make measurements of an unknown wavefront.

In the following section we will attempt to identify several dominant sources of error and to develop nomenclature for describing these effects and modeling the system behavior.

### 3.2.1. Centroid estimation error

The centroid estimation error is the primary measure of the repeatability of the system. It is non zero due to the finite signal to noise of real detector systems and other errors, such as CCD readout noise or synch jitter[17]. A measure of the centroid estimation error can be obtained by recording a large sequence of measurements and then analyzing the centroid positions. For a sequence of N measurements, and a sensor with K lenslets:

$$ v^2 = \frac{1}{N} \sum_{n=1}^{N} \left( \frac{1}{K} \sum_{k=1}^{K} (x_k - \bar{x}_k)^2 + (y_k - \bar{y}_k)^2 \right)_n \tag{10} $$

which results in the standard deviation of the centroids. This formula assumes that the *x* and *y* centroids, and the individual measurements in the sequence are statistically independent. In practice, this is not quite true due to the variation in the way the focal spots are sampled across the lenslet. Also it assumes that the statistical variations related to the instrument, and not to turbulence or other experimental setup effects.

### 3.2.2. Centroid pixelization error

Pixelization error is defined as the error caused by reducing the real irradiance distribution of each focal spot to a series of discrete measurements that represent the integral of the irradiance distribution over finite boundaries. This results in a loss of information which cannot be recovered[18]. This error is not dependent upon the signal-to-noise ratio of each individual element, but upon the sampling of the focal spot. For Shack-Hartmann sensors it is often the limiting factor on the total accuracy. To evaluate this error, the estimated position is compared to the real position of an ideal spot.

$$\sigma_{Px}^2 = \left\langle \left( \hat{x} - x_I \right)^2 \right\rangle \tag{11}$$

where the pixelization error $\sigma_{px}$ is determined by varying the focal spot locations $x_I$ in a known way and comparing against the estimated centroid locations $x$.

In general this error may be a function of the actual centroid location.
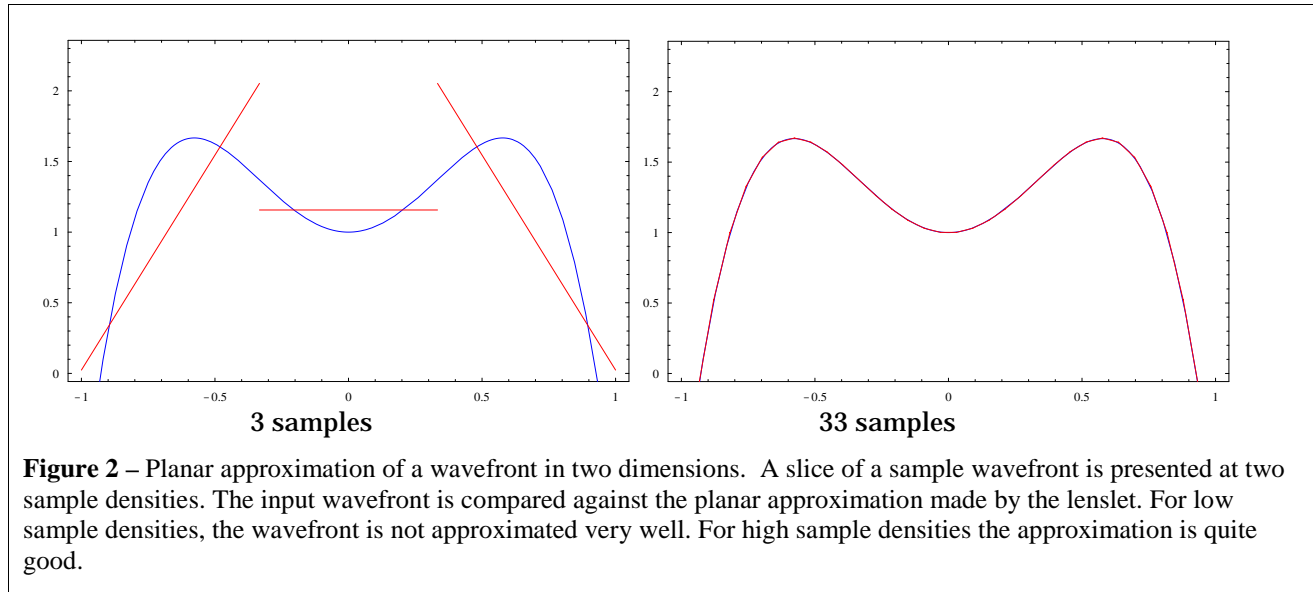
The pixelization factor is defined as:



3 samples                33 samples

**Figure 2** – Planar approximation of a wavefront in two dimensions. A slice of a sample wavefront is presented at two sample densities. The input wavefront is compared against the planar approximation made by the lenslet. For low sample densities, the wavefront is not approximated very well. For high sample densities the approximation is quite good.

$$K_p = \frac{\sigma_{Px}}{\upsilon} \tag{12}$$

### 3.2.3. Fitting error

The key assumption that underlies the wavefront sensor is that the wavefront is well represented by a piecewise planar approximation. This is because a lenslet measures the average wavefront slope across its aperture.

For a real wavefront, there is a fitting error between the piecewise planar approximation and the actual wavefront surface. Figure 2 shows an example of this effect. In Figure 2(a) the wavefront is very poorly approximated by the very low resolution lenslet array (3 lenslets across the aperture). There is a large fitting error between the actual wavefront and the lenslet array estimate. In Figure 2(b), however, there are 33 samples across the same wavefront. In this case the difference between the incident wavefront and the measured wavefront is insignificant. In
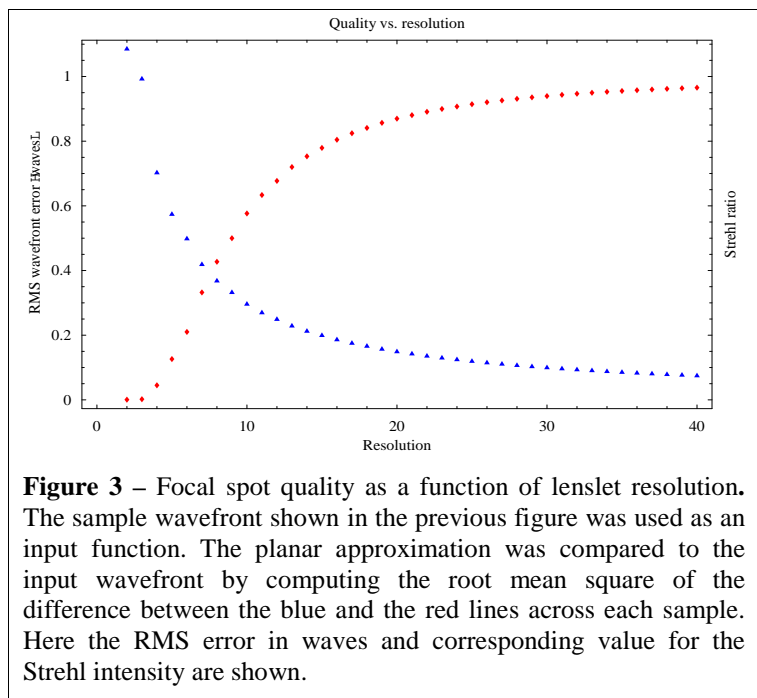


**Figure 3** – Focal spot quality as a function of lenslet resolution. The sample wavefront shown in the previous figure was used as an input function. The planar approximation was compared to the input wavefront by computing the root mean square of the difference between the blue and the red lines across each sample. Here the RMS error in waves and corresponding value for the Strehl intensity are shown.

Figure 3 this RMS difference is plotted as a function of the number of samples across the wavefront shown in Figure 2.

There is an additional effect for the case where the fitting error is large (i.e. a significant fraction of a wave). In this case the focal spot itself is degraded to the point where the centroid calculation suffers additional error. Also presented in Figure 3 is the resulting Strehl ratio of the focal spot. For this case, less than about 20 lenslets across the wavefront under test results in a significant reduction in the focal spot Strehl.

The errors associated with this effect are difficult to evaluate since they are wavefront dependent.

### 3.2.4. Gradient errors

While the essential information is obtained from the centroid locations, it is useful to define the errors in terms of the calculated wavefront gradients. In Eq. 2, while the fundamental aspects for determining the centroids arrive through the same calculation methods, the error is not the same for each term. Applying the method of variations to Eq. 2 results in:

$$\delta\beta_x = \frac{\delta x_c}{L_H} + \frac{\delta x_r}{L_H} \tag{13}$$

where the last term has been neglected, since it represents a calibration error and not a measurement error. For a given measurement using the wavefront sensor, these terms are not necessarily equal.

An accurate reference wave is an integral part of determining the accuracy of the sensor. To this end it is important to provide known reference waves. Typically an average is recorded over a fairly large number of frames. The



**Figure 4** –Experimental layout for measuring precision and accuracy of wavefront sensors.

accuracy of this reference wave depends upon the same factors as the other centroid estimation parameters. If the reference wave is recorded from a single frame of data, then the error terms in Eq. 13 are roughly equal. However, averaging over a large number of frames can result in a significant reduction in the second term, thereby reducing the total error nearly in half. Only the statistical fluctuation of the focal spot positions is important for the reference since any systematic effects, the result of any systematic differences in the reference centroid positions due to errors in the lenslet or detector array, are subtracted through the use of the difference in Eq. 2.

For sensors built around digital cameras with square pixels, the *x*- and *y*-directions are not generally different in the statistics of the error, and each focal spot results in (generally) statistically independent measurement of the *x*- and *y*- focal spot positions. For other cameras, due to differences in the pixel size or synchronization, these effects may be different. The RMS gradient error is defined as:

$$\beta_{RMS}^2 = \frac{\left(\sigma_{Px}^2 + \sigma_{Py}^2\right)}{L_H^2} + \frac{\left(\sigma_{x,REF}^2 + \sigma_{y,REF}^2\right)}{L_H^2} \tag{14}$$

The centroid estimation accuracy can be written in terms of this parameter as: $CEA = \beta_{RMS}f$.

### 3.2.5. Reconstructor noise factor

The wavefront slopes represent a wavefront surface with the addition of some finite amount of noise. The reconstructor can have the effect of damping this noise (through an averaging or fitting process) or of amplifying it. Thus the reconstructor factor is defined as how much the per lenslet wavefront error due to the centroiding and other factors is amplified or damped by the reconstructor. Hence a reconstructor factor can be defined as:
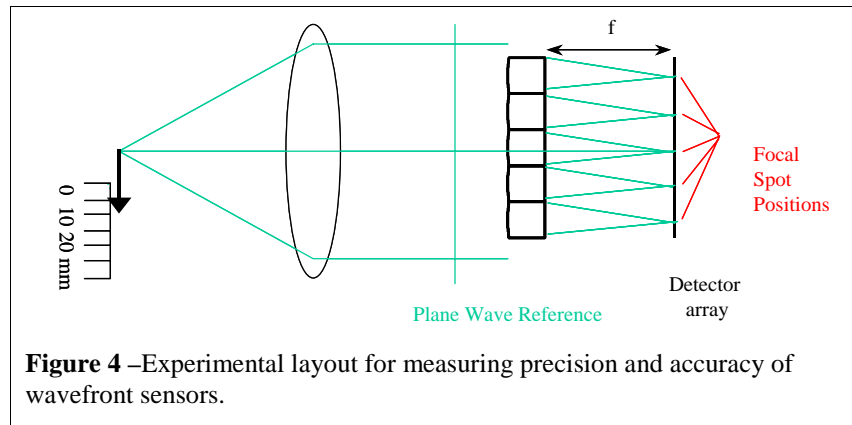
$$K_R = \frac{w_{RMS}}{\beta_{RMS}d} \tag{15}$$

where $w_{RMS}$ is the wavefront error RMS (usually with tilt removed) obtained from the reconstructed wavefront.

This model characterizes the way a given reconstructor amplifies the noise. Analysis of any given reconstructor can result in a measure of this factor and for scaling as a function of the number of samples[13].

## 4. MEASUREMENT OF WAVEFRONT SENSOR PERFORMANCE

These various factors can be measured for any given combination of lenslet array and detector. In this section experimental results will be presented for several different detector combinations. Three different sensor configurations were evaluated with a common camera as the detector element (Digital 10-bit Cohu 6612 with 640×480 9.9 μm pixels). The lenslet arrays had a constant Fresnel number ($N_F = d^2/f\lambda$) of 4.0, with the combinations $f/d$: 8.19/0.144, 2.05/0.072, and 25.09/0.252 (mm/mm).

### 4.1. Performance measurement methodology

The experimental setup is shown in Figure 4. A single mode fiber was used as a point source with a 500-mm focal length collimating lens (CVI AAP-500-101.6). The focal length of this lens is long enough that the irradiance distribution was extremely uniform over the

**Figure 5 -** RMS centroid locations (compared to the reference location, taken as the reference) (*x* and *y*) for a sequence of static measurements. The average is 0.0047 μm.

entire lenslet array. For the precision measurements, the fiber position was set for best collimation and zero tilt. For the accuracy measurements the position of the fiber was controlled using a computer-controlled stage that had position accuracy of 1 μm. This allowed tilt to be introduced in a precisely known manner and facilitated automated acquisition of multiple frames of data. The apparatus was completely enclosed to minimize air turbulence during data acquisition.

#### 4.1.1. Centroid Estimation Error

To measure the repeatability (or centroid estimation error) the fiber source was arranged at the point of best collimation and no tilt. This position was used for recording both the reference wave and the measurement data. The reference wave was constructed by recording and averaging 100 frames of data. All data analysis was performed using an 11% threshold to calculate the centroid in each AOI.

In Figure 5, a plot of the RMS Gradient as a function of time is presented. This is the measured slope error that is calculated using Eq. 2. While this plot shows the total gradients RMS values, it includes the errors in both the measurement frames and the reference frames. However, since only the difference is recorded for each frame, the exact distribution was not actually measured for this case. However, the reference, being obtained from a 100-frame average, has a very small contribution to the error in this case. Thus all of the error can be assigned to the measurement frames with little error, giving a centroid estimation error, ν, of 0.066 μm. The pixels for this camera are 9.9 μm square, so this represents 1/150th of a pixel.
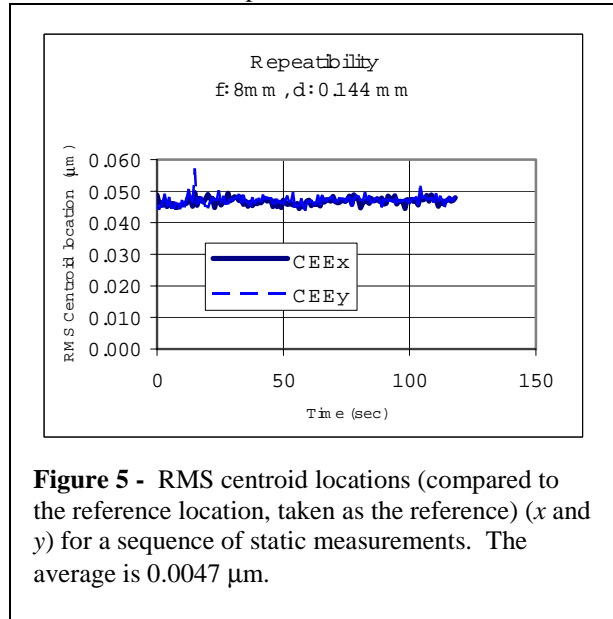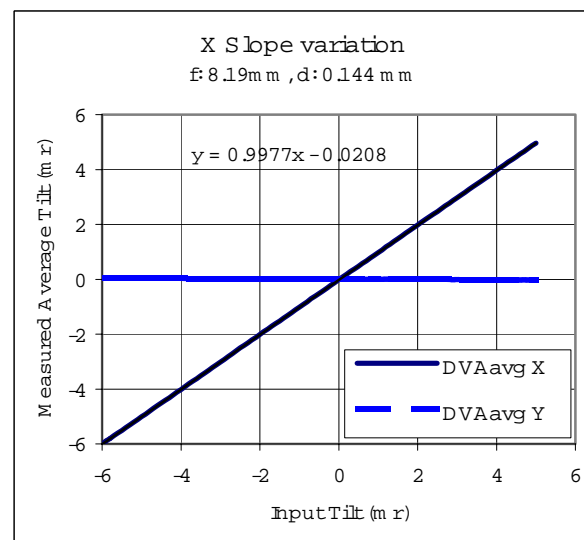
**Figure 6 –** Measured average tilt as a function of input tilt. This sensor is accurately calibrated, with a slope error of less than 0.2%

This is the repeatability for this system. It depends upon the number of digitization bits in the camera (10 for this case), the camera noise, readout noise and other statistical factors. The precision for this sensor is directly related to this quantity.

### 4.1.2. Pixelization factor

To determine the accuracy, it is necessary to vary some parameter in a known fashion. Using the apparatus of Figure 4 it is possible to vary the tilt in a systematic and rigorous manner. Figure 6 shows the resulting average tilt when the input tilt was varied in the *x*-direction. This sensor is accurately calibrated, with a slope error of 0.2%. Figure 7 shows the residual RMS error after subtracting the average tilt from each measurement. This plot shows that the error increased about three times compared to Figure 5. Clearly the addition of tilt has affected the accuracy of the measurement. For this sensor, once the tilt is sufficient to move the focal spot a significant fraction of a pixel, the RMS centroid error greatly increases. In this case a tilt sufficient to move the focal spot by one complete pixel is 1.27 mr. In Figure 7, this periodicity is evident in the *x*-component of the RMS values. The finite pixels sampling of the focal spot leads to different centroid results depending upon the exact alignment of the focal spot light with the camera pixels.

The reason for this becomes clear if the individual pixel samples are examined. Figure 10 shows the pixel values (for the same data as in Figure 7) as the focal spot is moved in ¼ pixel increments. Initially, the brightest two pixels appear to have almost the same value, with a slightly higher value on the right side of the peak. As the focal spot moves (to the left) it is sampled differently. So the distribution of values changes. In the 0.3 mr case the values are nearly equal. The 0.6 mr case is approximately ½ pixels, and the central brightest pixels have reversed, with the brightest now on the left. As the focal spot continues to move to the left it cyclically moves through the various patterns, repeating after one full pixel. The peak intensity will also vary slightly. For low-resolution systems (as compared to the focal spot) this pixelization effect becomes more pronounced, to the point where it can dominate the accuracy of the measurement. Even for this relatively well sampled array it is the dominant effect. Comparing Figure 7 and Figure 5, it is apparent that the RMS centroid error is 1.75 times larger except where the tilt is nearly zero. This effect is reduced for larger number of pixels across the focal spot, and enhanced for lower number. Since this is nearly constant for many sensors, this can be used to describe the accuracy compared to the precision of the sensor.
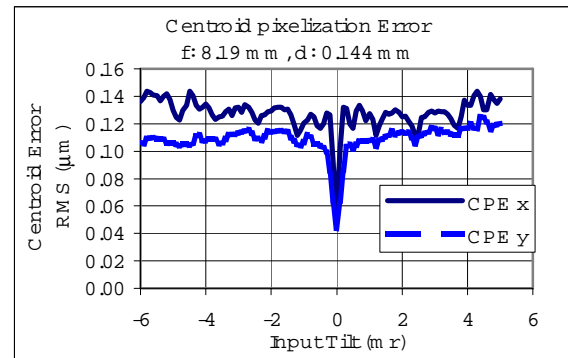


**Figure 7** – Residual RMS gradients (after removing the average tilt) for different input tilt values.
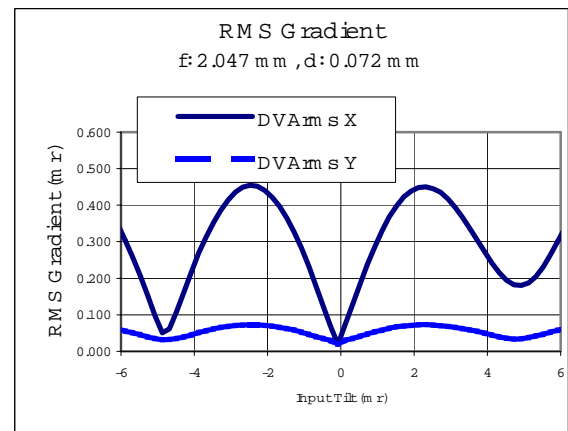


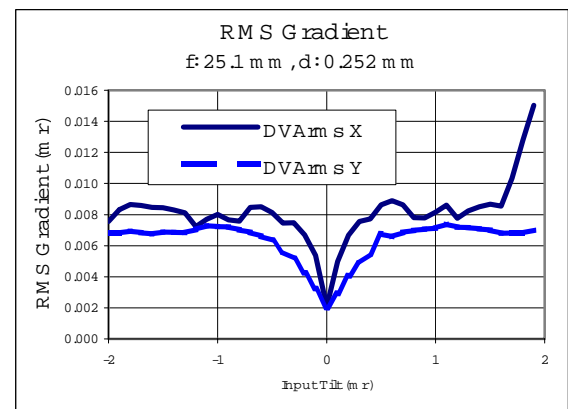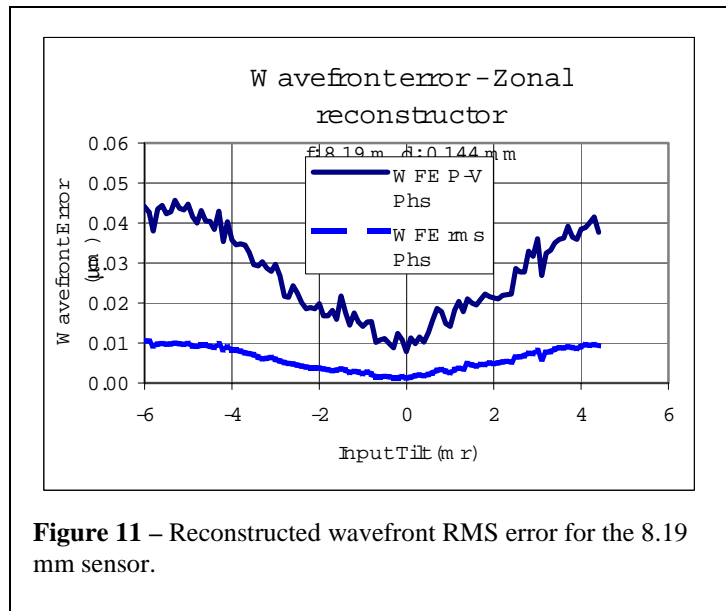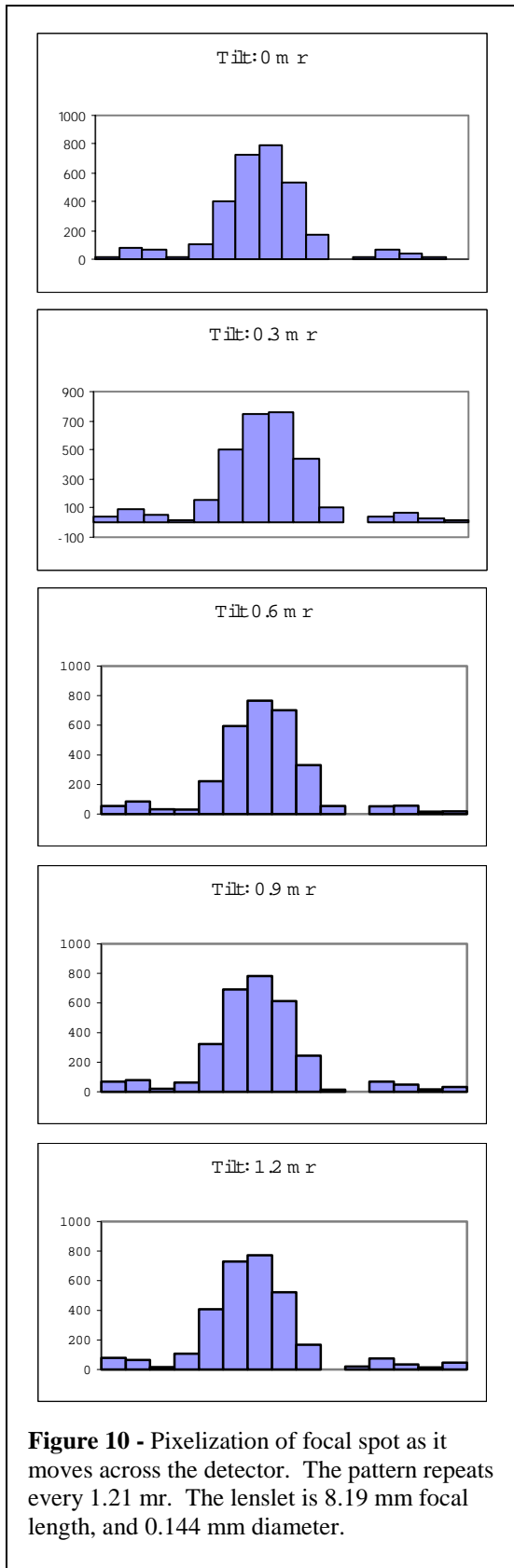**Figure 8 -** Centroid estimation error for 2 mm wavefront sensor.



**Figure 9 –** Slope error for a 25 mm focal length lenslet array

**Figure 10 -** Pixelization of focal spot as it moves across the detector. The pattern repeats every 1.21 mr. The lenslet is 8.19 mm focal length, and 0.144 mm diameter.



**Figure 11 –** Reconstructed wavefront RMS error for the 8.19 mm sensor.

While the reduction in accuracy due to pixelization is evident for the moderate resolution sensor of Figure 5, which has moderate resolution, for a lenslet array which covers a fewer number of pixels the effect is much stronger. In Figure 8, a lenslet array with half the lenslet size is shown. In this case the number of pixels under the focal spot is also ½ the number of the previous figures (in each direction). The effect is a strong periodic variation in the RMS wavefront error as the input tilt was varied. The periodicity is given by the pixel spacing of the camera. The accuracy is much worse than the precision, with the peak centroid estimation error 6.7 times worse than the precision and the average of 4.1 times larger. In fact, the ratio of the maximum to the minimum values in Figure 8 is about 25. The large variation in the gradient error as a function of tilt means that it is difficult to evaluate this sensor with zero tilt. Thus the repeatability is not measured with successive measurements near the minimum in the gradient error curve, but at some point slightly different than zero. Since the curve varies rapidly, any small variations in the true input tilt (caused by a slight amount of turbulence in the lab, or alignment drift) will result in a large average repeatability value, and hence lead to lower overall precision metrics. This, however, is an accurate assessment of the difficulty in making accurate and precise measurements with this very short focal length wavefront sensor. For this sensor it is still easy to achieve very good repeatability, but it does not have very good accuracy. However, this particular sensor has significantly more dynamic range. Both the number of lenslets is double in each direction and the angular dynamic range per lenslet is greater. Both of these factors contribute to the total wavefront error for the sensor.

As a final comparison, the gradient estimation error is shown for another sensor configuration using a 25 mm focal length, 0.252 mm diameter lenslet array. In this case, the focal spot covers three times as many pixels as in Figure 5. In this case one pixel corresponds to 0.39 mr. The RMS Gradient error

is maximum at 8 μr. However, the pixelization factor is still roughly the same at 3.96.

### 4.1.3. Reconstructor factor

Another factor that is important to measure is the effect of reconstructing the wavefront from the gradient measurements. If this serves to amplify the noise or attenuate it, then the reconstructor must be taken into account when evaluating the system performance.

The data of Figure 7 was reconstructed using the zonal reconstruction method of Eq. 4 and 5. The residual wavefront error (with tilt removed) is shown in Figure 11. In this plot both the peak-to-valley and RMS values are shown. Compared to Figure 7, the RMS error increases continuously with tilt, with up to a factor of five reduction of accuracy near the limits of the dynamic range for this sensor.



**Figure 12** – Accuracy factors for the f = 8.19 mm, d = 0.144 mm wavefront sensor.

It is interesting to note that the RMS wavefront error curve in Figure 11 does not follow the shape of the gradient error or centroid error curves (as shown in Figure 7). This is because the errors are not random, but correlated. The reconstructor can either attenuate or amplify these errors. However, for correlated errors, the response of the reconstructor depends upon the details of the correlated inputs. Thus the shape of the curve in Figure 11 differs from Figure 7 due to the particular correlation in the measurements.

The reconstructor and pixelization factors are shown in Figure 12 for the 8.19/0.144 mm sensor, as defined in Equations 12 and 15. It is evident that, for this particular combination of sensor elements, the pixelization factor is fairly constant over the range of measurements. However, the reconstructor factor follows more closely the RMS wavefront error plot of Figure 11. This indicates that the error model introduced in Equation 15 does not include all of the relevant phenomenon. However, the average of this factor (over all measurements that are within the specified dynamic range) is still a good indication of the average performance of the sensor. For this case the average reconstructor factor is about 1.8.

### 4.2. Lenslet array scaling

To develop scaling laws for use in designing new lenslet array/camera combinations, it is useful to determine how these error terms vary as a function of lenslet parameters. To this end, a number of different sensors were constructed using the same camera (Digital 10-bit Cohu 6612 with 640×480 9.9 μm pixels). Several different lenslet arrays were tested for accuracy and precision using the setup of Figure 4. These lenslet arrays had a constant design Fresnel number, $N_F = d^2/f\lambda = 4.0$ for all the arrays.

| Lenslet Focal Length | mm | 2.047 | 8.189 | 8.189 | 25.086 |
|---|---|---|---|---|---|
| Lenslet Size | mm | 0.072 | 0.144 | 0.144 | 0.252 |
| Centroid Estimation Error (um) | um | 0.160 | 0.049 | 0.066 | 0.065 |
| Centroid Accuracy | um | 0.757 | 0.201 | 0.167 | 0.250 |
| RMS WFE per Lenslet | um | 0.0266 | 0.0025 | 0.0029 | 0.0025 |
| Pixelization Factor | | 4.1 | 2.9 | 2.5 | 3.8 |
| Average Recon Factor (zonal) | | 0.7 | 1.8 | 1.3 | 0.9 |

**Table 1** – Comparison of the performance for several different wavefront sensors with Fresnel number = 4.0.

Table 1 presents a summary of these results for a few different lenslet arrays. In this table, two different 8.19 mm lenslets are shown to show repeatability of the accuracy measurement.
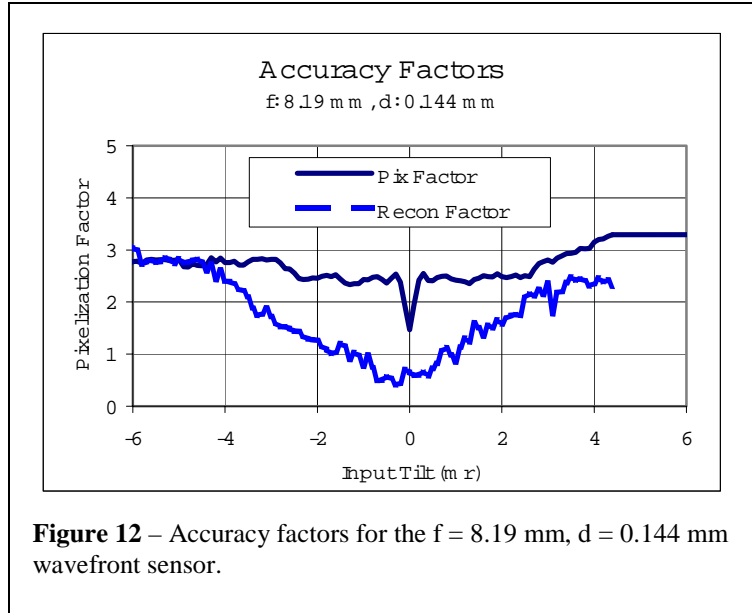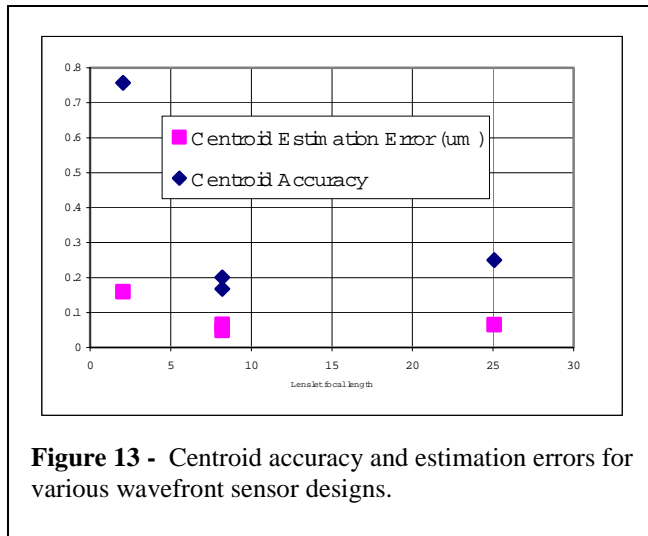
**Figure 13 -** Centroid accuracy and estimation errors for various wavefront sensor designs.
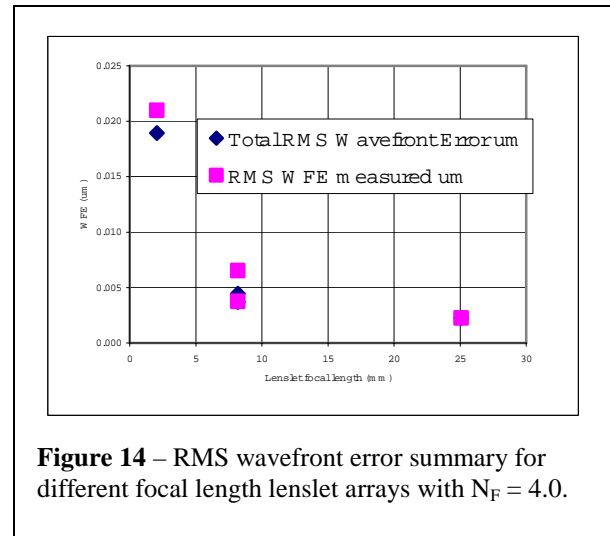


**Figure 14** – RMS wavefront error summary for different focal length lenslet arrays with $N_F = 4.0$.

The total centroid estimation error and centroid accuracy error are shown in Figure 13. While there is a dramatic decrease in the error between the 2 mm and 8.19 mm sensors, the centroid estimation errors are about the same (or slightly increased) for the 25 μm sensor. This is surprising considering that the lenslet array has both three times as many pixels and three times the focal length. The resulting wavefront error, as shown in Figure 14, does decrease, but not nearly as much as would be expected by the increased focal length. However, the resulting total RMS wavefront error is extremely small for the long focal length lenslet arrays. Thus other errors, such as errors in the test wavefront caused by diffraction from dust or fabrication errors, would be expected to have a larger effect. In fact, some such errors were apparent in the data for the 25 mm focal length sensor.

## 5. CONCLUSIONS

We have identified a method for measuring the performance of different wavefront sensors and for making comparisons of different designs. The average performance was evaluated over the dynamic range of each sensor and average performance metrics identified. Key parameters such as centroid estimation error, centroid estimation accuracy, and RMS wavefront error were identified.

For short focal length lenslet arrays the pixelization can be the dominant factor in the overall accuracy. However, other factors play a role for sensor with a longer lenslet focal length.

These results will help with the development of scaling laws for the design of new sensors and for comparison of the performance of various different wavefront sensor designs.

## 6. REFERENCES

[1] B. Platt, R. Shack, "History and principles of Shack-Hartmann wavefront sensing" *Journal of Refractive Surgery*, **17** (Sept/Oct 2001).

[2] D. R. Neal, W. J. Alford, and J. K. Gruetzner, "Amplitude and phase beam characterization using a two-dimensional wavefront sensor", *SPIE* **2870,** pp.72-82 (1996).

[3] D. R. Neal, J. K. Gruetzner, D. M. Topa, J. Roller, "Use of beam parameters in optical component testing," *SPIE* **4451**, pp. 394–405 (2001).

[4] D. R. Neal, D. J. Armstrong and W. T. Turner, "Wavefront sensors for control and process monitoring in optics manufacture," *SPIE* **2993**, pp. 211–220 (1997).

[5] R. R. Rammage, D. R. Neal, R. J. Copland, "Application of Shack-Hartmann wavefront sensing technology to transmissive optic metrology," *SPIE* **4779**-27 (2002).

[6] J. Liang, B. Grimm, S. Goelz, and J. F. Bille, "Objective measurement of the wave aberrations of the human eye with the use of a Hartmann-Shack wave-front sensor," *J. Opt. Soc. Am. A* **11**, pp. 1949–1957 (1994).

[7] S. Panagopoulou, "Correction of high order aberrations using WASCA in LASIK for myopia," Fall World Refractive Surgery Symposium, Dallas, TX (October 19–21, 2000).

[8] S. MacRae, J. Schwiegerling, and R. Snyder, "Customized Corneal Ablation and Super Vision," *J. Ref. Surg.* **16**, S230-235 (2000).

[9] T. D. Raymond, D. R. Neal, and D. M. Topa, "High-speed, non-interferometric nanotopographic characterization of Si wafer surfaces," *SPIE* **4809**-34 (2002).

[10] See for example, "Diffractive and Miniaturized Optics," Sing Lee, ed., *SPIE* **CR49** (1993).

[11] *ISO 15367-2*. Note: we have tried to follow the nomenclature of the new ISO standard for Hartmann-Shack wavefront sensors as much as much as possible.

[12] D. R. Neal, D. M. Topa and J. Copland, "The effect of lenslet resolution on the accuracy of ocular wavefront measurements," *SPIE* **4245**, pp. 78–91 (2001).

[13] W. Southwell, Wave-front estimation from wave-front slope measurements, *J. Opt. Soc. Am.* **70**(8), (1980).

[14] W. Jiang, H. Xian, F. Shen, "Detecting error of Shack-Hartmann wavefront sensor," *SPIE* **312**6, pp. 534–544 (1997).

[15] H. Suzuki, J. Suzuki, T. Matshushita, and S. Wakabayashi, "Error analysis of a Shack-Hartmann wavefront sensor," *SPIE* **2443**, pp. 798–805 (1995).

[16] J. Pfund, N. Lindlein, and J. Schwider, "Misalignment effects of the Shack-Hartmann sensor," *Appl Opt.* **37**(1), pp. 22–27 (1998).

[17] G. Cao, X. Yu, "Accuracy analysis of a Hartmann-Shack wavefront sensor operated with a faint object," *Opt. Eng.* **33**, pp. 2331-2335 (1994).

[18] J. Arines and J. Ares, "Minimum variance centroid thresholding," *Optics Letters* **27**(7), pp. 497–499 (April 1, 2002).